

# 1 Dynamics of Ice/Water Confined in Nanoporous Alumina

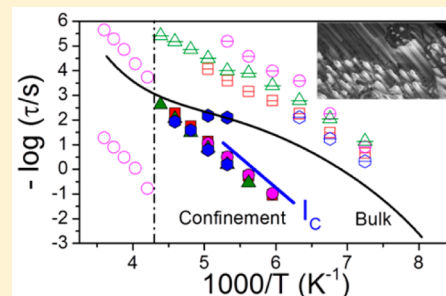
2 Yasuhito Suzuki,<sup>†</sup> Martin Steinhart,<sup>‡</sup> Robert Graf,<sup>†</sup> Hans-Jürgen Butt,<sup>†</sup> and George Floudas<sup>\*,§</sup>

3 <sup>†</sup>Max-Planck Institute for Polymer Research, 55128 Mainz, Germany

4 <sup>‡</sup>Institut für Chemie neuer Materialien, Universität Osnabrück, D-49069 Osnabrück, Germany

5 <sup>§</sup>Department of Physics, University of Ioannina, 45110 Ioannina, Greece

6 **ABSTRACT:** Dielectric (DS), IR spectroscopy, and <sup>1</sup>H MAS NMR are  
7 employed in the study of ice/water confined in nanoporous alumina with pore  
8 diameters ranging from 400 nm down to 25 nm. Within nanoporous alumina  
9 there is a transformation from heterogeneous nucleation of hexagonal ice in the  
10 larger pores to homogeneous nucleation of cubic ice in the smaller pores. DS and  
11 IR show excellent agreement in the temperature interval and pore size  
12 dependence of the transformation. DS further revealed two dynamic processes  
13 under confinement. The “fast” and “slow” processes with an Arrhenius  
14 temperature dependence are attributed to ice and supercooled water relaxation,  
15 respectively. The main relaxation process of ice under confinement (“slow”  
16 process) has an activation energy of  $44 \pm 2$  kJ/mol. The latter is in agreement  
17 with the reported relaxation times and activation energy of cubic ice prepared following a completely different route (by  
18 pressure). <sup>1</sup>H MAS NMR provided new insight in the state of ice structures as well as of supercooled water. Under confinement,  
19 a layer of liquid-like water coexists with ice structures. In addition, both ice structures under confinement appear to be more  
20 ordered than bulk hexagonal ice. Supercooled water in the smaller pores is different from bulk water. It shows a shift of the signal  
21 toward higher chemical shift values which may suggest stronger hydrogen bonding between the water molecules or increasing  
22 interactions with the AAO walls.



## I. INTRODUCTION

23 Water—the most important liquid by any standard of  
24 judgment—behaves differently under confinement. Although  
25 the subject is fundamental and of considerable intrinsic  
26 importance in science and technology, it remains under-  
27 represented in research because of the lack of well-defined  
28 confining media. Recently,<sup>1</sup> we employed self-ordered nano-  
29 porous aluminum oxide (AAO) as confining medium. AAO  
30 contains arrays of discrete, parallel, and cylindrical nanopores  
31 with uniform pore length and diameter as a model system to  
32 study the effect of confinement on water crystallization. We  
33 found indications for a transformation from heterogeneous  
34 nucleation of hexagonal ice ( $I_h$ ) to homogeneous nucleation of  
35 predominantly cubic ice ( $I_c$ ) with decreasing AAO pore  
36 diameter. Furthermore, inside AAO with pores having  
37 diameters  $\leq 35$  nm no sign was found for the monotropic  $I_c$   
38  $\rightarrow I_h$  transition commonly observed upon heating. Our results  
39 lead to the phase diagram of water under confinement at  
40 atmospheric conditions. It contains a predominant  $I_c$  form, a  
41 form known to exist as such only in the upper atmosphere.<sup>1</sup>  
42 Subsequently, the kinetics of ice nucleation confined inside  
43 AAO was investigated.<sup>2</sup> This study explored the stochastic  
44 nature of both heterogeneous and homogeneous nucleation  
45 and further provided the respective temperature intervals of  
46 metastability.

47 Despite good knowledge of the effect of confinement on the  
48 nucleation mechanism/kinetics of ice nucleation, the dynamics  
49 of supercooled water have not been investigated within the  
50 same AAO nanopores. Earlier studies on the dynamics of

supercooled water investigated the fragile-to-strong liquid  
51 transformation,<sup>3</sup> as well as the dynamics under confinement  
52 in clays,<sup>4</sup> in silica matrices,<sup>15</sup> in polymeric matrices,<sup>16</sup> and in  
53 nanoporous membranes, both by experiment<sup>4–16</sup> and by  
54 computer simulations,<sup>17–20</sup> the latter under severe confinement  
55 conditions. Other studies explored the coupling of water and  
56 protein dynamics in hydrated proteins.<sup>21–23</sup> On the other hand,  
57 the dynamics of ice, and in particular, the temperature  
58 dependence of relaxation times  $\tau(T)$ —explored mainly with  
59 dielectric spectroscopy—are not well understood.<sup>23–31</sup> There is  
60 consensus, however, that the rich dynamics of ice reflects  
61 certain properties of the hydrogen bonding network. The  
62 arrangement of water molecules in ice follows the Bernal-  
63 Fowler-Pauling rules<sup>32,33</sup> that give rise to an open ice lattice.  
64 These rules impose constraints on the reorientational motion of  
65 water molecules in the most well-known ice structure, that of  $I_h$ .  
66 Bulk ice  $I_h$  relaxation investigated as a function of temperature  
67 exhibits three characteristic temperature regimes with two  
68 corresponding crossovers.<sup>23,25,26</sup> The high temperature cross-  
69 over is distinct in the  $\tau(T)$  dependence ( $T \sim 230$  K), but this is  
70 not true for the crossover at lower temperatures ( $T \sim 170$  K).  
71 Therefore, attempts have been made to explain the origin of the  
72 high temperature dynamic crossover. Bjerrum proposed<sup>34</sup> an  
73 orientation mechanism for the dielectric relaxation and  
74 conductivity of  $I_h$  crystals that violates the Bernal-Fowler-  
75

Received: September 8, 2015

Revised: October 27, 2015

76 Pauling rules and produce two kinds of orientational defects:  
 77 one with a pair of neighboring O...O atoms missing a hydrogen  
 78 (L-defect) and one with a pair of neighbors O–H H–O, i.e.,  
 79 with two hydrogen atoms (D-defect). Water molecules can  
 80 reorient by the diffusion of L and D defects. Different ideas  
 81 have been proposed to explain the dynamic crossover. In one, it  
 82 was suggested that the crossover reflects the reorientation of a  
 83 single molecule at higher temperatures and a concerted  
 84 reorientation of several molecules at lower temperatures.<sup>25</sup> A  
 85 second approach attributed the crossover to a decrease in  
 86 concentration of intrinsically generated defects by decreasing  
 87 temperature.<sup>26</sup> Lastly, a more recent approach<sup>29</sup> discussed the  
 88 competition of L/D orientational defects with the generation  
 89 and migration of ionic defects (generated through the  
 90 Grotthuss mechanism) that dominate at higher and inter-  
 91 mediate temperatures, respectively.

92 Herein we investigate the dynamics of ice formed within  
 93 AAO templates as a function of pore diameter and temperature.  
 94 DS, IR, and <sup>1</sup>H MAS NMR techniques are employed to explore  
 95 the temperature interval and pore size dependence of the  
 96 transformation from the supercooled liquid to ice. Subse-  
 97 quently, DS is employed in studying the effect of confinement  
 98 on ice dynamics. Since in the smaller pores, the only stable ice  
 99 structure is I<sub>c</sub>, the current system allows an investigation of I<sub>c</sub>  
 100 dynamics in the absence of high pressure conditions. The effect  
 101 of confinement is discussed with respect to the temperature  
 102 dependence of relaxation times,  $\tau(T)$ , and the broadening of  
 103 relaxation spectra. Results on the dynamics are compared with  
 104 recent relaxation experiments on I<sub>c</sub> prepared under pressure.  
 105 Furthermore, <sup>1</sup>H MAS NMR explores the possibility of a liquid  
 106 layer of water as well as the similarity of supercooled water in  
 107 the smaller pores with bulk water.

## II. EXPERIMENTAL SECTION

108 **Dielectric Spectroscopy (DS).** Dielectric measurements  
 109 were performed either under isochronal conditions (at a  
 110 frequency of 1 MHz) as a function of temperature in the range  
 111 from 183 to 303 K, or under “isothermal” conditions using a  
 112 Novocontrol Alpha frequency analyzer (frequency range from  
 113 10<sup>-2</sup> to 10<sup>6</sup> Hz). For the water infiltrated self-ordered AAO  
 114 samples, a 10 mm electrode was placed on top of the templates,  
 115 whereas the Al in the bottom of the templates served as the  
 116 second electrode. The measured dielectric spectra were  
 117 corrected for the geometry by using two capacitors in parallel  
 118 (composed of  $\epsilon^*_{\text{W}}$  and  $\epsilon^*_{\text{A}}$ , being the complex dielectric  
 119 function of water and alumina, respectively). The measured  
 120 total impedance was related to the individual values through 1/  
 121  $Z^* = 1/Z^*_{\text{W}} + 1/Z^*_{\text{A}}$ . This equation allows calculation of the  
 122 real and imaginary parts of the dielectric permittivity as a  
 123 function of the respective volume fractions by using  $\epsilon^*_{\text{M}} =$   
 124  $\epsilon^*_{\text{W}}\phi_{\text{W}} + \epsilon^*_{\text{A}}\phi_{\text{A}}$ . The complex dielectric permittivity  $\epsilon^* = \epsilon' -$   
 125  $i\epsilon''$ , where  $\epsilon'$  is the real and  $\epsilon''$  is the imaginary part, is a  
 126 function of frequency  $\omega$ , temperature  $T$ , and in general pressure  
 127  $P$ ,  $\epsilon^* = \epsilon^*(\omega, T, P)$ . In the analysis of the DS spectra we have  
 128 used the empirical equation of Havriliak and Negami (HN)<sup>35,36</sup>

$$\epsilon_{\text{HN}}^*(\omega, T) = \epsilon_{\infty}(T) + \frac{\Delta\epsilon(T)}{[1 + (i\omega\tau_{\text{HN}}(T))^m]^n} + \frac{\sigma_0(T)}{i\epsilon_f\omega} \quad (1)$$

129 where  $\tau_{\text{HN}}(T, P)$  is the characteristic relaxation time,  $\Delta\epsilon(T, P)$   
 130  $= \epsilon_0(T, P) - \epsilon_{\infty}(T, P)$  is the relaxation strength of the process  
 131 under investigation,  $m, n$  (with limits  $0 < m, mn \leq 1$ ) describe,

132 respectively, the symmetrical and unsymmetrical broadening of  
 133 the distribution of relaxation times,  $\sigma_0$  is the dc-conductivity  
 134 and  $\epsilon_f$  is the permittivity of the free space. In the fitting  
 135 procedure, we have used the  $\epsilon''$  values at every temperature,  
 136 and in some cases the  $\epsilon'$  data were also used as a consistency  
 137 check. From  $\tau_{\text{HN}}$  the relaxation time at maximum loss,  $\tau_{\text{max}}$  is  
 138 obtained analytically following:  
 139

$$\tau_{\text{max}} = \tau_{\text{HN}} \cdot \sin^{-1/m} \left( \frac{\pi m}{2(1+n)} \right) \cdot \sin^{1/m} \left( \frac{\pi mn}{2(1+n)} \right) \quad (2)$$

Note that for  $n = 1$ , the process is symmetric in a logarithmic  
 141 representation and known as the Cole–Cole function.<sup>35,36</sup> In  
 142 the latter case, the characteristic relaxation time coincides with  
 143 the dielectric loss maximum. In the temperature range where  
 144 two relaxation processes contribute to  $\epsilon^*$  there are two ways of  
 145 representing the data. The first one, followed here, is based on a  
 146 summation of two HN functions and assumes statistical  
 147 independence in the frequency domain. The second one,  
 148 proposed by Williams and Watts is a molecular theory for the  
 149 dipole moment time-correlation function  $C_{\mu}(t)$  (also known as  
 150 “Williams ansatz”).<sup>37</sup> An alternative representation of the  
 151 dielectric data is through the inverse of the dielectric  
 152 permittivity  $\epsilon^*(\omega)$ , i.e., the electric modulus, which is related  
 153 to the dielectric permittivity through  
 154

$$M^*(\omega) = \frac{1}{\epsilon^*(\omega)} = M' + iM'' \quad (3)$$

In eq 3,  $M'$  and  $M''$  are the real and imaginary parts of the  
 156 electric modulus, respectively.  
 157

**IR Measurements.** Infrared spectra were measured using a  
 158 Fourier transform infrared spectrometer (Nicolet Magna IR  
 159 850). The AAO templates were filled with a mixture of 10%  
 160 D<sub>2</sub>O in H<sub>2</sub>O. Due to fast proton exchange HOD is the  
 161 predominant deuterated water species in the samples (18%  
 162 HOD and 1% D<sub>2</sub>O). The AAO templates were placed in a  
 163 cryostat (Oxford Instruments GF 1204) with a nitrogen  
 164 atmosphere allowing for thermal equilibration. Temperature  
 165 was reduced by cooling the cryostat jacket and thus the  
 166 nitrogen gas in the cryostat. To ensure thermal equilibration,  
 167 temperature was measured at the sample holder. Following a  
 168 minimum of 30 min equilibration, the transmission IR spectra  
 169 were recorded.  
 170

**<sup>1</sup>H MAS NMR Spectroscopy.** <sup>1</sup>H MAS NMR spectroscopy  
 171 measurements have been performed with a Bruker Avance III  
 172 console operating at 850 MHz <sup>1</sup>H Larmor frequency in the  
 173 temperature range between 230 and 290 K at 20 kHz MAS  
 174 spinning frequency. The measurements have been performed  
 175 using a commercial MAS double resonance probe supporting  
 176 2.5 mm MAS rotors. The temperature has been calibrated using  
 177 the temperature dependent <sup>79</sup>Pb chemical shift of lead nitrate as  
 178 described in the literature. A Bruker BCU II cooling unit has  
 179 been used with a VT gas flow of 1500 L/h. The <sup>1</sup>H MAS NMR  
 180 signals have been recorded using the EASY scheme, in order to  
 181 suppress the <sup>1</sup>H probe back and the ringing artifacts of the rf  
 182 coil.  
 183

## III. RESULTS AND DISCUSSION

The dielectric permittivity and IR absorbance of water and its  
 184 temperature dependence were employed as a fingerprint of the  
 185 mechanism of ice nucleation. Figure 1a compares the dielectric  
 186 permittivity curves ( $\epsilon'_{\text{M}}$  values are shown in Figure 1a) of bulk  
 187 water with water inside AAO with pore diameters of 400, 35,  
 188

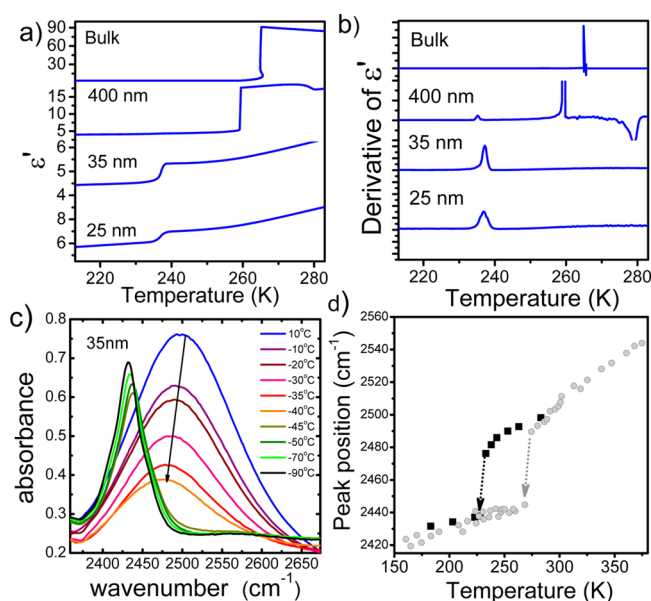


**Figure 1.** Summary of ice nucleation inside AAO templates from dielectric spectroscopy (top) and IR (bottom). (a) Dielectric permittivity of bulk water and of water inside AAOs with different pore diameters obtained on cooling (rate 5 K/min) at a frequency of 1 MHz. Steps at low and high supercooling signify ice formation via heterogeneous and homogeneous nucleation, respectively. (b) Derivative of dielectric permittivity as a function of temperature. The vertical dotted line indicates the temperature of homogeneous nucleation. (c) Infrared absorption spectra of a mixture containing 10%  $D_2O$  in  $H_2O$  inside AAO with a pore diameter of 35 nm at frequencies characteristic of the OD stretching vibration. At temperatures higher than 233 K the OD stretching vibration is broad and has nearly a Gaussian line shape. At temperatures lower than 228 K a narrow absorption band is observed at  $2430\text{ cm}^{-1}$  characteristic of ice. (d) Peak maximum of the OD absorption band obtained using a Gaussian function (at temperatures above 233 K) or a Lorentzian function (at temperatures below 233 K) on top of a constant background. The gray symbols are literature values<sup>39</sup> for neat water/hexagonal ice.

189 and 25 nm under isochronal conditions ( $f = 1\text{ MHz}$ ). Figure 1b  
190 shows the derivative of dielectric permittivity with respect to  
191 temperature as a function of temperature. The latter quantity is  
192 sensitive to phase transformations. These curves show a  
193 discontinuous decrease of  $\epsilon'(T)$  at 260 K attributed to the  
194 heterogeneous nucleation of water inside AAO with a pore  
195 diameter of 400 nm. These findings suggest that the majority of

400 nm pores contain *impurities* that initiate crystallization by  
heterogeneous nucleation. In addition, wall-induced nuclea-  
tion—being proportional to the pore surface—is more  
significant in the larger pores. Crystallization in the smaller  
pores is fundamentally different.<sup>1</sup> Only a single step in dielectric  
permittivity is observed in the range from 237 to 235 K.  
Therefore, in AAO with pore diameters of 35 or 25 nm, water  
crystallizes practically exclusively by homogeneous nucleation.  
Confinement within AAO alters the ice nucleation mechanism  
and affects the crystal structure. Ice nucleated within AAO  
templates with the larger pores is the common hexagonal ice  $I_h$ .  
However, in the smaller pores X-ray diffraction indicated that  
predominantly cubic ice ( $I_c$ ) is formed. This form is stable  
under annealing and persists up to the melting point.<sup>1</sup> The  
stabilization of ice  $I_c$  within the smaller pores facilitates a study  
of the dynamics under ambient pressure conditions (see  
below).

Figure 1c displays the infrared absorption spectra at  
frequencies characteristic of the OD stretching vibration of  
HOD molecules. At ambient conditions the OD stretching  
band is centered at  $\sim 2500\text{ cm}^{-1}$  and has a Gaussian line shape,  
indicative of inhomogeneous broadening. Upon cooling the  
intensity of the band is significantly reduced down to a  
temperature of 233 K. This reduction likely reflects some  
unavoidable evaporation during the experiment. While cooling,  
the broad nature of the absorption band is maintained down to  
233 K, indicative of supercooled liquid water. At the same time,  
the band shifts to lower frequencies in line with expectation  
from bulk water (Figure 1d).<sup>38,39</sup> At temperatures below 233 K  
the OD stretching band becomes much narrower and red-shifts  
to  $\sim 2430\text{ cm}^{-1}$ . The Lorentzian band shape at these  
temperatures is indicative of a phase transformation to  
crystalline ice.<sup>39,40</sup> The band position, extracted from fitting  
with a Lorentzian function, is shown in Figure 1d. The peak  
shifts to lower wavenumbers with decreasing temperature and  
closely resembles the peak positions that have been reported  
for hexagonal ice.<sup>39</sup> The red-shift of the OD absorption band of  
supercooled water and ice with decreasing temperature is  
indicative of enhanced intermolecular interaction (hydrogen  
bond strength). The increase in intensity upon decreasing  
temperature—a feature also present in bulk hexagonal ice—can  
be explained from an increased absorption cross-section due to  
enhanced intermolecular interaction.<sup>40</sup> The stronger the H-  
bond, the larger the transition dipole moment of the OD  
stretching vibration and the larger the absorption cross section.  
We note that the studied OD stretching vibration is not

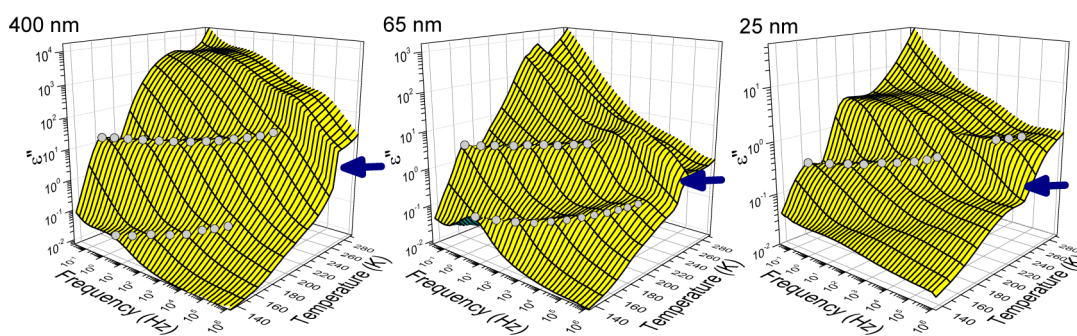


**Figure 2.** Dielectric loss curves in a 3D representation for water located inside AAOs with different pore sizes. Gray dots indicate the frequency position of the main process of ice relaxation under confinement. Arrows indicate the respective crystallization temperatures at  $\sim 260\text{ K}$  and  $\sim 235\text{ K}$  for water within 400 nm, and within 65 nm and 25 nm pores, respectively.

242 sensitive to the symmetry of the crystal structure (the IR  
243 spectra of hexagonal and cubic ice are very similar).<sup>41</sup> Thus,  
244 while the IR spectra clearly show ice nucleation inside AAOs,  
245 the band-shape does not allow for determination of the exact  
246 crystalline phase of ice. Nevertheless, there is full quantitative  
247 agreement between IR and DS with respect to the temperature  
248 of transformation from a heterogeneous nucleation mechanism  
249 in the larger pores to a homogeneous nucleation mechanism in  
250 the smaller pores.

251 The dielectric loss spectra for water located inside AAO  
252 templates as a function of frequency for a range of temperatures  
253 are discussed with respect to Figure 2. They all show a  
254 discontinuous decrease of the dielectric loss curves whose  
255 magnitude and exact temperature are a function of AAO pore  
256 diameter. This was anticipated from the “isochronal” dielectric  
257 permittivity data of Figure 1a. For example, for water located  
258 inside AAO with pores of 400 nm in diameter the  
259 discontinuous change occurs at  $\sim 260$  K, whereas inside pores  
260 with diameters of 65 and 25 nm it occurs at  $\sim 235$  K. As we  
261 discussed with respect to Figure 1 this reflects a different  
262 mechanism of ice nucleation: from heterogeneous nucleation of  
263 hexagonal ice within the 400 nm pores to homogeneous  
264 nucleation of predominantly cubic ice within the smaller pores.  
265 Furthermore, the curves depict at least two processes on the  
266 high frequency side and a more intense process at lower  
267 frequencies.

268 For the analyses of the dynamics under confinement a  
269 summation of two Cole–Cole processes was necessary. Some  
270 representative fits for the dielectric loss spectra at  $T = 183$  K are  
271 shown in Figure 3. The data for bulk ice are from ref 24. It

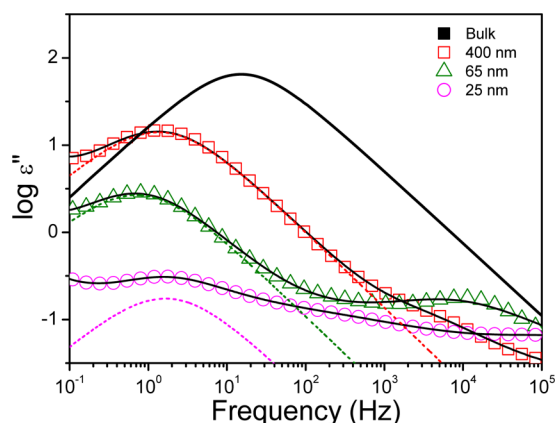


Figure 3. Dielectric loss curves of ice in the bulk (from ref 24) and inside AAO with different pore diameters. All data refer to 183 K. Black lines are fits to a single HN (bulk) or to a summation of two HN processes. Dashed lines give the slower process for ice within AAO.

272 depicts a single albeit non-Debye process. The effect of  
273 confinement is threefold: first, the main process shifts to lower  
274 frequencies (i.e., becomes slower on confinement). Second, the  
275 process is broadened, and third, another faster process appears  
276 at higher frequencies. In addition, the main process for ice  
277 within 400 nm AAO is coupled to the process of ionic  
278 conductivity (extracted from the crossing frequency of the real  
279 and imaginary parts in the  $\epsilon^*$ ,  $M^*$ , or  $\sigma^*$  representations).<sup>36</sup> In  
280 the smaller pores the process due to ionic conductivity is slower  
281 than the process corresponding to the maximum of the  
282 dielectric loss. This possibly suggests a different mechanism of  
283 ice relaxation in the smaller pores.

The low frequency shape parameter for the main ice process 284  
is plotted in Figure 4 as a function of temperature for some 285

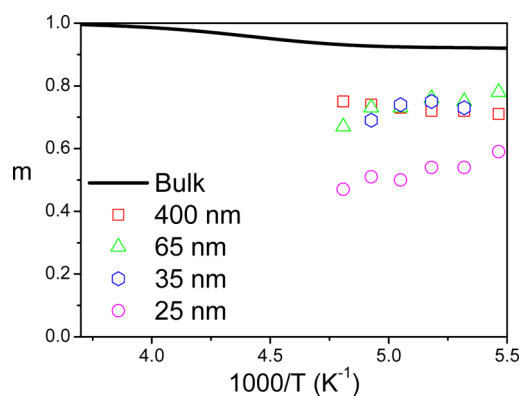


Figure 4. Temperature dependence of the Cole–Cole shape parameter of the main process corresponding to bulk ice (solid line from ref 23) and to ice located inside AAO. There is a significant broadening of the dynamics of ice on confinement.

AAO pore diameters. In the bulk, measurements on ice single 286  
crystals revealed a single relaxation process of the Cole–Cole 287  
type ( $n = 1$ ) or Debye type ( $m = n = 1$ ), respectively, at 288  
temperatures below and above 250 K.<sup>29,23</sup> For ice located inside 289  
AAO, the distribution of relaxation times for the main process 290  
is broad and furthermore depends on the pore size. 291  
Confinement results in a variety of environments that leads 292  
to the broadening of the relaxation spectra. 293

In the bulk, the relaxation spectrum found within  $I_h$  was 294  
attributed to the presence of impurities that generate 295  
orientational defects.<sup>26</sup> These defects were thought to be 296  
spatially heterogeneous, i.e., different regions relax with 297  
different rates. Apart from the distribution of relaxation times, 298  
the characteristic frequency at maximum loss, and in particular, 299  
its temperature dependence has been a point of debate. Figure 300  
5 shows literature data<sup>26</sup> (solid line in Figure) of bulk ice  $I_h$  301  
relaxation as a function of temperature. It depicts three 302  
characteristic temperature regimes. At high temperatures ice 303  
relaxes via an Arrhenius temperature dependence with an 304  
activation energy of  $\sim 53$  kJ/mol. At intermediate temperatures 305  
it follows another Arrhenius dependence with an activation 306  
energy of  $\sim 19$  kJ/mol. At lower temperatures the activation 307  
energy increases again to  $\sim 46$  kJ/mol. The ideas proposed to 308  
explain the dynamic crossover were based on either L/D 309  
orientational defects<sup>25,26</sup> and/or to the migration of ionic 310  
defects.<sup>29</sup> 311

The dynamics of ice located inside AAOs is depicted in 312  
Figure 5 together with the ice data in the bulk. Interestingly, the 313  
main process under confinement has an Arrhenius temperature 314  
dependence with an activation energy  $E \sim 44 \pm 2$  kJ/mol, i.e., 315  
similar to bulk ice but corresponding to the high temperature 316  
region. This could suggest the dominance of orientational L/D 317  
defects under confinement. Moreover, a faster process exists 318  
under confinement with a lower activation energy ( $E \sim 28 \pm 2$  319  
kJ/mol for the 65 nm case). 320

Additional information on the origin of dynamic processes 321  
can be obtained by comparing the dynamics under confinement 322  
within AAOs with recent studies of  $I_c$  produced via 323  
pressure.<sup>30,31</sup> The results, shown with a blue line in Figure 5, 324  
include an Arrhenius process corresponding to the relaxation of 325  
 $I_c$ . Interestingly, the relaxation times of  $I_c$  produced via 326

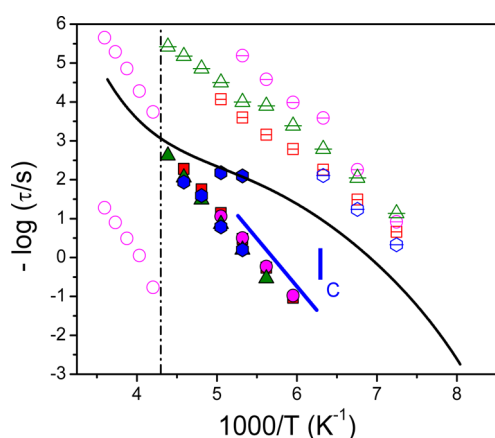


**Figure 5.** Relaxation times at maximum loss for bulk ice (solid line is from ref 26) and for ice/water confined in AAO based on fitting with a summation of two Cole–Cole functions: (squares), 400 nm; (up triangles), 65 nm; (hexagons), 35 nm; and (circles), 25 nm pores. Filled symbols correspond to the main relaxation process on confinement, half-filled symbols to a faster relaxation, and empty symbols to the relaxation of undercooled water inside 25 nm AAO pores. The vertical dash-dotted line at 235 K is the temperature of homogeneous nucleation in the smaller pores. The blue line corresponds to the dynamics of cubic ice from ref 30.

327 homogeneous nucleation within AAO templates at ambient  
 328 pressure are located in the vicinity of the  $I_c$  produced under  
 329 pressure following a totally different path (it includes certain  
 330 ultraviscous liquids; one of low density and one of high  
 331 density).<sup>30,31</sup> In this latter case,  $I_c$  was metastable to  $I_h$  and fully  
 332 transformed to it on heating. On the contrary, the  $I_c$  structure  
 333 obtained in confinement is the thermodynamically stable phase.  
 334 Nevertheless, the dynamics within  $I_c$  are only dependent on the  
 335 ice structure and not on the particular path that it is employed.  
 336 The dielectric strength of the main relaxation process under  
 337 confinement is also of interest as it relates to the local ordering  
 338 around a given dipole. Based on the Kirkwood–Fröhlich  
 339 equation<sup>35,36</sup>

$$\frac{(\epsilon'_s - \epsilon_\infty) \cdot 3 \cdot (2\epsilon'_s + \epsilon_\infty)}{\epsilon'_s(\epsilon_\infty + 2)^2} = \frac{1}{3\epsilon_0} \cdot g \cdot \frac{\mu_0^2}{k_B T} \cdot \frac{N_0}{V} \quad (4)$$

341 where  $\epsilon'_s$  is the measured dielectric permittivity,  $\epsilon_\infty$  is to the  
 342 permittivity value in the limit of high frequencies where any  
 343 intrinsic dipolar relaxation is inactive,  $\epsilon_0$  ( $=8.85 \times 10^{-12}$  F/m) is  
 344 the permittivity of vacuum;  $N_0/V$  is the number density of  
 345 dipoles expressed as  $(\rho/M)N_A$ , where  $\rho$  is the mass density and  
 346  $M$  is the molar mass; and  $\mu_0$  is the gas-phase dipole moment. In  
 347 the present case the dielectric strength,  $\Delta\epsilon = \epsilon'_s - \epsilon_\infty$ , has been  
 348 normalized by the porosity. In the equation,  $g$  is the Kirkwood–  
 349 Fröhlich dipole orientation correlation function,  $g = \mu^2/\mu_{\text{gas}}^2$ ,  
 350 defined as the ratio of the mean-squared dipole moment  
 351 measured in a dense system and within a spherical region  
 352 surrounding a test dipole divided by the same quantity for the  
 353 test dipole obtained in a noninteracting case. As such,  $g$ , is a  
 354 measure of local ordering in the absence of any external field; a  
 355 value of 1 signifies that fixing the position of a single dipole  
 356 does not influence the remaining dipoles surrounding the test  
 357 dipole. On the other hand, a value of  $g > 1$  ( $g < 1$ ) signifies that  
 358 fixing the test dipole tends to align its neighbors in  
 359 predominantly parallel (antiparallel) orientation. The calcula-  
 360 tion of the Kirkwood–Fröhlich factor is very sensitive<sup>42</sup> to the  
 361 actual value for  $\epsilon_\infty$  (a limiting value at high frequencies of  $\epsilon_\infty \sim$

3.2, or the optical frequency limiting value of  $\epsilon_\infty = n^2$ , where  $n$  362  
 = 1.33 is the refractive index for  $I_h$ ). Employing the optical 363  
 frequency limiting value and  $\rho = 917 \text{ kg/m}^3$  results in  $g \sim 3.3$  364  
 for bulk  $I_h$ . Upon confinement, a similar value is obtained (i.e.,  $g$  365  
 $\sim 2.7$ ) for ice nucleated within the 400 nm pores with the  $I_h$  366  
 structure. However, within the smaller pores the dielectric 367  
 permittivity is a decreasing function of temperature (whereas 368  
 the opposite trend is observed for bulk undercooled water<sup>43</sup>). 369  
 By following the kinetics of crystallization as a function of 370  
 temperature we attributed the distinct  $\epsilon'_s(T)$  dependence to 371  
 water reorganization acting as a precursor to crystallization.<sup>2</sup> 372  
 The strong reduction in dielectric permittivity for water located 373  
 inside the smaller pores precludes extracting a definitive value 374  
 for the dipole orientation correlation function. We mention 375  
 here that Monte Carlo simulations suggested a similar value of 376  
 $g$  for  $I_c$  and  $I_h$ .<sup>44</sup> 377

In addition to this process, the faster process under 378  
 confinement has rates and activation energies intermediate to 379  
 the ultraviscous low- and high-density liquid processes obtained 380  
 under pressure.<sup>30,31</sup> Moreover, the process is in the vicinity of 381  
 interfacial supercooled water under hard confinement.<sup>45</sup> Based 382  
 on these findings we assign the faster process to some 383  
 undercooled interfacial water, whereas the slower and more 384  
 intense process to the relaxation of predominantly  $I_c$ . The fact 385  
 that there exists some undercooled water is already evident 386  
 from the dielectric permittivity values of Figure 1a. 387

More insight into the presence of a liquid layer of water can 388  
 be obtained from  $^1\text{H}$  NMR. This is shown in Figure 6 where 389 66

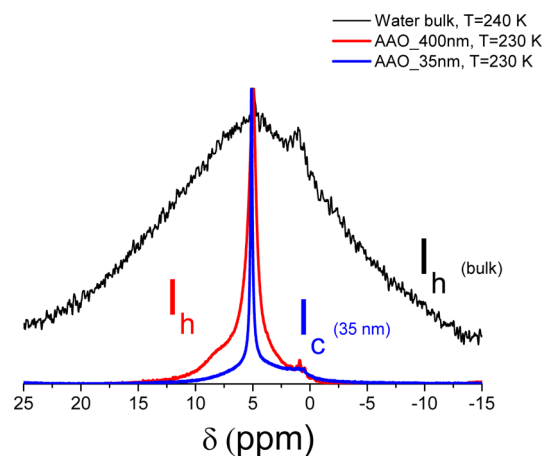


**Figure 6.** MAS spectra at a Larmor frequency of 20 kHz for bulk hexagonal ice at 240 K (black line), and for water located inside AAOs with pore diameter of 400 nm (red line) and 35 nm (blue line) at 230 K.

the  $^1\text{H}$  MAS NMR spectra of bulk hexagonal ice and of water 390  
 within AAOs with pore diameters of 400 and 35 nm are 391  
 compared at 240 and 230 K, respectively. Under confinement, a 392  
 narrow signal around 5 ppm is observed which results from a 393  
 layer of liquid-like water coexisting with ice structures. In 400 394  
 nm pores the signal of the liquid-like water is significantly 395  
 broader compared to the signal of the sample with 35 nm 396  
 pores. The line width of the liquid-like water is determined by 397  
 width of the chemical shift distribution of possible environ- 398  
 ments as well as by the exchange rates of the individual 399  
 molecules between those different environments. Thus, the 400  
 local environments of the liquid-like water within 35 nm pores 401  
 is much more homogeneous, compared to that in the 400 nm 402

403 pores. Moreover the NMR signal of the  $I_h$  ice structure in the  
 404 400 nm pore sample is observed as a broad peak at an average  
 405 chemical shift  $\delta \geq 5$  ppm. In AAO with 35 nm pore size the  
 406 NMR signal of the  $I_c$  structure is significantly more narrow and  
 407 is observed in the spectrum at an average chemical shift  $\delta \leq 5$   
 408 ppm. Both ice structures under confinement appear to be more  
 409 ordered than bulk hexagonal ice, as indicated by the  
 410 substantially narrower chemical shift distribution of the former.

411 In addition,  $^1\text{H}$  MAS NMR measurements provide valuable  
 412 information on the state of supercooled water in the smaller  
 413 pores. The question here is how similar (or different)  
 414 supercooled water within pores is when compared to bulk  
 415 water. Despite the fact that bulk water is measured at 275 K,  
 416 whereas undercooled water is measured at 250 K, it can be seen  
 417 (Figure 7) that the line width of supercooled water within the

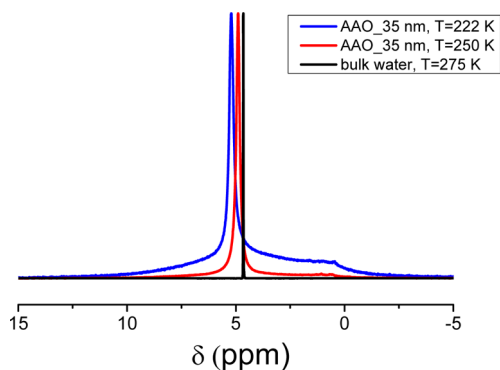


**Figure 7.** MAS spectra at a Larmor frequency of 20 kHz for bulk water at 275 K and for supercooled water located inside AAO with a pore diameter of 35 nm recorded at 250 K (red line) and of water/ice mixture at 222 K (blue line).

418 35 nm pores is significantly broader as compared to that of bulk  
 419 water. The line width of liquid water is determined by the  
 420 chemical shift distribution of all populated states of water  
 421 molecules in the liquid state, as well as from the exchange rate  
 422 of the molecules between those different states. Moreover,  
 423 differences in the dipolar dephasing efficiency of water, typically  
 424 expressed as T2 relaxation time, will contribute to the line  
 425 width of liquid water. At  $T = 222$  K, predominantly cubic ice—  
 426 as determined by X-ray diffraction studies—coexists with  
 427 liquid-like water of reduced mobility. Going from bulk water  
 428 at 275 K to confined water at 250 K and to 222 K, the NMR  
 429 signal of the liquid-like water shifts toward higher ppm values  
 430 with decreasing temperature. The shift of the signal toward  
 431 higher chemical shift values indicates an electronic deshielding  
 432 of the time and ensemble averaged  $^1\text{H}$  sites, which may result  
 433 from a stronger hydrogen bonding between the water  
 434 molecules or from increasing interactions with the AAO walls.

#### IV. CONCLUSION

435 Confining water within AAO pores results in a transformation  
 436 from heterogeneous nucleation of hexagonal ice in the larger  
 437 pores to homogeneous nucleation of predominantly cubic ice in  
 438 the smaller pores. The cubic ice thus formed is the equilibrium  
 439 crystal structure. Dielectric and IR spectroscopy agree in  
 440 identifying the temperature interval and pore size dependence  
 441 of the transformation. In addition, dielectric spectroscopy  
 442 revealed that confinement significantly alters the dynamics.  
 443 This is manifested in the bimodal relaxation, the broadening of  
 444 relaxation spectra, the slower dipolar dynamics, and the weaker

dipolar orientational correlations. The main relaxation process  
 445 under confinement has an activation energy of  $44 \pm 2$  kJ/mol.  
 446 The relaxation times and activation energy of this process agree  
 447 with the relaxation times and activation energy within  $I_c$ , the  
 448 latter prepared through a completely different route. This  
 449 agreement of dynamics suggests some unique features of cubic  
 450 ice irrespective of “preparation” method (confinement vs  
 451 pressure).  
 452

$^1\text{H}$  MAS NMR measurements provided new insight in the  
 453 state of ice structures as well as of supercooled water. Under  
 454 confinement, a narrow signal around 5 ppm is observed which  
 455 results from a layer of liquid-like water coexisting with ice  
 456 structures. In addition, both ice structures under confinement  
 457 appear to be more ordered than bulk hexagonal ice. Supercooled  
 458 water in the smaller pores is different from bulk water. It shows  
 459 a shift of the signal toward higher chemical shift values which  
 460 may suggest stronger hydrogen bonding between the water  
 461 molecules or increasing interactions with the AAO walls.  
 462  
 463

#### AUTHOR INFORMATION

##### Corresponding Author

\*E-mail: gfloudas@uoi.gr.

##### Notes

The authors declare no competing financial interest.

#### ACKNOWLEDGMENTS

The current work was supported by the operational program of  
 470 the NSRF “Aristeia” cofinanced by the European Union and the  
 471 Greek state. AAO template preparation by C. Hess and H.  
 472 Tobergte are gratefully acknowledged. We thank J. Hunger and  
 473 M. Bonn (MPI-P) for several discussions and W. Scholdei for  
 474 the IR measurements.  
 475

#### REFERENCES

- (1) Suzuki, Y.; Duran, H.; Steinhart, M.; Kappl, M.; Butt, H.-J.; Floudas, G. Homogeneous Nucleation of Predominantly Cubic Ice Confined in Nanoporous Alumina. *Nano Lett.* **2015**, *15*, 1987–1992.
- (2) Suzuki, Y.; Steinhart, M.; Butt, H.-J.; Floudas, G. Kinetics of Ice Nucleation Confined in Nanoporous Alumina. *J. Phys. Chem. B* **2015**, *119*, 11960–11966.
- (3) Ito, K.; Moynihan, C. T.; Angell, C. A. Thermodynamic Determination of Fragility in Liquids and a Fragile-to-strong Liquid Transition in Water. *Nature* **1999**, *398*, 492–495.
- (4) Bergman, R.; Swenson, J.; Börjesson, L.; Jacobsson, P. Dielectric Study of Supercooled 2D Water in a Vermiculite Clay. *J. Chem. Phys.* **2000**, *113*, 357–363.
- (5) Vasilyeva, M. A.; Gusev, Y. A.; Shtyrilin, V. G.; Greenbaum (Gutina), A.; Puzenko, A.; Ishai, P. B.; Feldman, Y. Dielectric Relaxation of Water in Clay Minerals. *Clays Clay Miner.* **2014**, *62*, 62–73.
- (6) Sjöström, J.; Swenson, J.; Bergman, R.; Kittaka, S. Investigating Hydration Dependence of Dynamics of Confined Water: Monolayer, Hydration Water and Maxwell-Wagner Processes. *J. Chem. Phys.* **2008**, *128*, 154503.
- (7) Elamin, K.; Jansson, H.; Kittaka, S.; Swenson, J. Different Behavior of Water in Confined Solutions of High and Low Solute Concentrations. *Phys. Chem. Chem. Phys.* **2013**, *15*, 18437–18444.
- (8) Bruni, F.; Mancinelli, R.; Ricci, M. A. Multiple Relaxation Processes Versus the Fragile-to-strong Transition in Confined Water. *Phys. Chem. Chem. Phys.* **2011**, *13*, 19773–19779.
- (9) Fedichev, P. O.; Menshikov, L. I.; Bordonskiy, G. S.; Orlov, A. O. Experimental Evidence of the Ferroelectric Phase Transition Near the  $\lambda$ -Point in Liquid Water. *JETP Lett.* **2011**, *94*, 401–405.

- 506 (10) Faraone, A.; Liu, L.; Mou, C. Y.; Yen, C. W.; Chen, S. H.  
507 Fragile-to-Strong Liquid Transition in Deeply Supercooled Confined  
508 Water. *J. Chem. Phys.* **2004**, *121*, 10843–10846.
- 509 (11) Liu, L.; Chen, S. H.; Faraone, A.; Yen, C. W.; Mou, C. Y.  
510 Pressure Dependence of Fragile-to-Strong Transition and a Possible  
511 Second Critical Point in Supercooled Confined Water. *Phys. Rev. Lett.*  
512 **2005**, *95*, 117802.
- 513 (12) Tombari, E.; Johari, G. P. On the State of Water in 2.4 nm  
514 Cylindrical Pores of MCM from Dynamic and Normal Specific Heat  
515 Studies. *J. Chem. Phys.* **2013**, *139*, 064507.
- 516 (13) Johari, G. P. Origin of the Enthalpy Features of Water in 1.8 nm  
517 Pores of MCM-41 and the Large  $C_p$  Increase at 210 K. *J. Chem. Phys.*  
518 **2009**, *130*, 124518.
- 519 (14) Sattig, M.; Vogel, M. Dynamic Crossovers and Stepwise  
520 Solidification of Confined Water: A  $^2\text{H}$  NMR Study. *J. Phys. Chem.*  
521 *Lett.* **2014**, *5*, 174–178.
- 522 (15) Sattig, M.; Reutter, S.; Fujara, F.; Werner, M.; Buntkowsky, G.;  
523 Vogel, M. NMR Studies on the Temperature-dependent Dynamics of  
524 Confined Water. *Phys. Chem. Chem. Phys.* **2014**, *16*, 19229–19240.
- 525 (16) Colosi, C.; Costantini, M.; Barbetta, A.; Cametti, C.; Dentini, M.  
526 Anomalous Debye-like Dielectric Relaxation of Water in Micro-Sized  
527 Confined Polymeric Systems. *Phys. Chem. Chem. Phys.* **2013**, *15*,  
528 20153–20160.
- 529 (17) Menzl, G.; Köfinger, J.; Dellago, C. Phase Transition and  
530 Interpore Correlations of Water in Nanopore Membranes. *Phys. Rev.*  
531 *Lett.* **2012**, *109*, 020602.
- 532 (18) Köfinger, J.; Hummer, G.; Dellago, C. Macroscopically Ordered  
533 Water in Nanopores. *Proc. Natl. Acad. Sci. U. S. A.* **2008**, *105*, 13218–  
534 13222.
- 535 (19) Köfinger, J.; Hummer, G.; Dellago, C. Single-file Water in  
536 Nanopores. *Phys. Chem. Chem. Phys.* **2011**, *13*, 15403–15417.
- 537 (20) Dellago, C.; Naor, M. M. Dipole Moment of Water Molecules  
538 in Narrow Pores. *Comput. Phys. Commun.* **2005**, *169*, 36–39.
- 539 (21) Pagnotta, S. E.; Cervený, S.; Alegría, A.; Colmenero, J. The  
540 Dynamical Behavior of Hydrated Glutathione: a Model for Protein-  
541 Water Interactions. *Phys. Chem. Chem. Phys.* **2010**, *12*, 10512–10517.
- 542 (22) Chen, S.-H.; Liu, L.; Fratini, E.; Baglioni, P.; Faraone, A.;  
543 Mamontov, E. Observation of Fragile-to-strong Dynamic Crossover in  
544 Protein Hydration Water. *Proc. Natl. Acad. Sci. U. S. A.* **2006**, *103*,  
545 9012–9016.
- 546 (23) Shinyashiki, N.; Yamamoto, W.; Yokoyama, A.; Yoshinari, T.;  
547 Yagihara, S.; Kita, R.; Ngai, K. L.; Capaccioli, S. Glass Transitions in  
548 Aqueous Solutions of Protein (Bovine Serum Albumin). *J. Phys. Chem.*  
549 *B* **2009**, *113*, 14448–14456.
- 550 (24) Auty, R. P.; Cole, R. H. Dielectric Properties of Ice and Solid  
551  $\text{D}_2\text{O}$ . *J. Chem. Phys.* **1952**, *20*, 1309.
- 552 (25) Johari, G. P.; Jones, S. J. Dielectric Properties of Polycrystalline  
553  $\text{D}_2\text{O}$  Ice Ih (hexagonal). *Proc. R. Soc. London, Ser. A* **1976**, *349*, 467.
- 554 (26) Johari, G. P.; Whalley, E. The Dielectric Properties of Ice  $\text{I}_h$  in  
555 the Range 272–133 K. *J. Chem. Phys.* **1981**, *75*, 1333.
- 556 (27) Kawada, S. Dielectric Properties of Heavy Ice  $\text{I}_h$  ( $\text{D}_2\text{O}$  Ice). *J.*  
557 *Phys. Soc. Jpn.* **1979**, *47*, 1850–1856.
- 558 (28) Kawada, S. Dielectric Anisotropy in Ice  $\text{I}_h$ . *J. Phys. Soc. Jpn.* **1978**,  
559 *44*, 1881–1886.
- 560 (29) Popov, I.; Puzenko, A.; Khamzin, A.; Feldman, Y. The Dynamic  
561 Crossover in Dielectric Relaxation Behavior of Ice  $\text{I}_h$ . *Phys. Chem.*  
562 *Chem. Phys.* **2015**, *17*, 1489–1497.
- 563 (30) Amann-Winkel, K.; Gainaru, C.; Handle, P. H.; Seidl, M.;  
564 Nelson, H.; Böhmer, R.; Loerting, T. Water's Second Glass Transition.  
565 *Proc. Natl. Acad. Sci. U. S. A.* **2013**, *110*, 17720–17725.
- 566 (31) Loerting, T.; Fuentes-Landete, V.; Handle, P. H.; Seidl, M.;  
567 Amann-Winkel, K.; Gainaru, C.; Böhmer, R. The Glass Transition in  
568 High-density Amorphous Ice. *J. Non-Cryst. Solids* **2015**, *407*, 423–430.
- 569 (32) Bernal, J. D.; Fowler, R. H. The Theory of Water and Ionic  
570 Solution, with Particular Reference to Hydrogen and Hydroxyl ions. *J.*  
571 *Chem. Phys.* **1933**, *1*, 515.
- 572 (33) Pauling, L. The Structure and Entropy of Ice and Other Crystals  
573 with Some Randomness of Atomic Arrangements. *J. Am. Chem. Soc.*  
574 **1935**, *57*, 2680.
- (34) Bjerrum, N. Structure and Properties of Ice. *Science* **1952**, *115*, 575  
576 38.
- (35) Kremer, F.; Schoenhals, A. *Broadband Dielectric Spectroscopy*; 577  
Springer: Berlin, 2002. 578
- (36) Floudas, G. In *Polymer Science: A Comprehensive Reference*; 579  
Matyjaszewski, K., Möller, M., Eds.; Elsevier BV, 2012; Vol. 2.32. 580
- (37) Williams, G.; Watts, D. C. *NMR Basic Principles and Progress*, 581  
1971; Vol. 4. 582
- (38) Perakis, F.; Hamm, P. Two-dimensional Infrared Spectroscopy 583  
of Supercooled Water. *J. Phys. Chem. B* **2011**, *115*, 5289–5293. 584
- (39) Ford, T. A.; Falk, M. Hydrogen-bonding in Water and Ice. *Can.* 585  
*J. Chem.* **1968**, *46*, 3579–3586. 586
- (40) Li, F.; Skinner, J. L. Infrared and Raman Line Shapes for Ice  $\text{I}_h$ . I. 587  
Dilute HOD in  $\text{H}_2\text{O}$  and  $\text{D}_2\text{O}$ . *J. Chem. Phys.* **2010**, *132*, 204505–11. 588
- (41) Ockman, N. The Infra-red and Raman Spectra of Ice. *Adv. Phys.* 589  
**1958**, *7*, 199–220. 590
- (42) Andersson, O.; Inaba, A. Dielectric Properties of High-density 591  
Amorphous ice under pressure. *Phys. Rev. B: Condens. Matter Mater.* 592  
*Phys.* **2006**, *74*, 184201–10. 593
- (43) Bertolini, D.; Cassettari, M.; Salvetti, G. The Dielectric 594  
Relaxation Time of Supercooled Water. *J. Chem. Phys.* **1982**, *76*, 595  
3285–3290. 596
- (44) Adams, D. J. Theory of the Dielectric Constant of Ice. *Nature* 597  
**1981**, *293*, 447–449. 598
- (45) Swenson, J.; Cervený, S. Dynamics of Deeply Supercooled 599  
Interfacial Water. *J. Phys.: Condens. Matter* **2015**, *27*, 033102. 600